J Solid State Electrochem (2012) 16:2759–2766
DOI 10.1007/s10008-012-1699-2

ORIGINAL PAPER

Electrochemical performance and stability of nano-particulate and bi-continuous $La_{1-X}Sr_XCoO_3$ and $Ce_{0.9}Gd_{0.1}O_{1.95}$ composite electrodes

Per Hjalmarsson · Jonathan Hallinder · Mogens Mogensen

Received: 3 January 2012 / Revised: 16 February 2012 / Accepted: 18 February 2012 / Published online: 3 March 2012

Abstract A bi-continuous porous cathode consisting of nano-particles of strontium substituted lanthanum cobaltite (LSC) covering the surface of a $Ce_{0.9}Gd_{0.1}O_{1.95}$ (CGO10) backbone has been produced. The polarization resistance (R_P) of this cathode was measured to ~35 mΩ cm^2 at 650 °C. The area-specific resistance at 650 °C (ASR) when applied onto an anode supported cell (ASC) was found to increase from 540 to 730 mΩ cm^2 when subjected to a thermal cycle to 850 °C. This effect was attributed to particles coarsening but also to a reaction with the electrolyte. The results imply that a CGO10 barrier is required for this type of nano-structured cathode.

Introduction

Perovskite type oxides such as $(La_{1-x}Sr_x)_sMnO_{3+\delta}$ (LSM), $(La_{1-x}Sr_x)_sFeO_{3-\delta}$ (LSF) and $(La_{1-x}Sr_x)_sCoO_{3-\delta}$ (LSC) have been studied extensively as materials for SOFC cathode applications [1]. A specifically interesting material is LSC due to its good mixed ionic and electronic (MIEC) conducting properties and its high catalytic activity towards oxygen reduction [2, 3]. Unfortunately, its reactivity toward $(Y_2O_3)_{0.08}(ZrO_2)_{0.92}$ (8YSZ) forms the insulating products $SrZrO_3$ and $La_2Zr_2O_7$ and prevents the direct use of LSC on the conventional 8YSZ electrolyte [4]. Additionally, the comparably high thermal expansion coefficient (TEC) of LSC results in an expansion mismatch between the cathode and the rest of the cell that may cause mechanical rupture during the fabrication process or thermal cycling of the SOFC stack [5].

This paper presents data measured on an electrode structure that is built up of a thin layer of LSC particles covering the surface of a porous backbone of CGO10. Such a structure reduces the tensile strain induced by the *TEC* mismatch as the tensile stress decreases with layer thickness. Furthermore, a porous CGO10 backbone offers the possibility to substantially increase the surface area of the LSC thin film and thus the electrode area active for oxygen reduction. The suggested structure finally provides two full percolated phases as both CGO10 and LSC are formed sequentially and not randomly which is favorable in terms of electronic and oxide ion transport. The electrochemical performance of such a structure has been described earlier [6].

The thin film is typically prepared by infiltrating dissolved cations followed by sintering carried out, either prior to or in situ during test. The procedure results in nano-particles adhering to the backbone surface. The method has previously been applied to produce LSM:YSZ composite cathodes by infiltrating LSM into a porous YSZ scaffold [7]. Additionally, it has been shown that nano-particles of $Ce_{1-x}Y_xO_{2-\delta}$ [7, 8] infiltrated into conventional LSM:YSZ cathodes can significantly reduce its polarization resistance. There is also work reported on LSC [6], LSCF [9, 10], and $Sm_{0.5}Sr_{0.5}CoO_3$ (SSC) [11] infiltrated into porous CGO backbones with excellent electrochemical performance. These three compositions are all known to react with YSZ at elevated temperatures, preventing YSZ to be used as the backbone material. In conventional SOFCs with MIEC oxygen electrodes made of the aforementioned materials, an inter-diffusion barrier of CGO is used. This additional layer makes manufacturing and sintering more complex and costly.

P. Hjalmarsson (✉) · J. Hallinder · M. Mogensen
Risø National Laboratory for Sustainable Energy,
Technical University of Denmark,
Fredrikborgsvej 399, P.O. Box 49, DK-4000 Roskilde, Denmark
e-mail: phja@risoe.dtu.dk

The infiltrated electrodes are different from the conventional counterparts in several aspects: (1) The sintering temperature of infiltrated electrodes is substantially lower than for conventionally sintered ones. (2) The loading of the electro-catalytic compound is low. (3) The electro-catalyst is to a very low degree in direct contact with YSZ only if the entire thickness of the electrode becomes infiltrated. It is therefore of technological relevance to study the performance of such an electrode when applied directly onto the YSZ electrolyte.

Infiltrated electrodes are conceptually new structures that have only recently received attention and the reasons why synthesizing nano-particles within the electrode structure have such a positive effect are still unclear [12, 13]. This paper does not attempt to answer this question but tries to address this question by discussing experimental results on electrodes fabricated by infiltrating and sintering LSC within a porous film of CGO10.

Experimental

Powder of CGO10 (Rhodia, France) was dispersed into an ink and screen printed onto both sides of a 200 μm thick and 50×50 mm^2 large, commercial (Kerafol, Germany) sintered CGO10 tape (cell A) and 8YSZ ($(Y_2O_3)_{0.08}(ZrO_2)_{0.92}$) tape (cell B). Cell A and cell B were sintered at 1,150 °C which results in an approximate porosity of 64 % and thickness of 50 μm [6]. The symmetrical cells were cut into samples of an approximately nominal area of 5×5 mm^2. Samples from cell A and cell B were subsequently infiltrated with an aqueous solution consisting of a surfactant (P-123, BASF) and metal nitrates with a cation molar ratio corresponding to the nominal composition $(La_{0.6}Sr_{0.4})_{0.99}CoO_3$. The infiltration was repeated 6 times with intermediate heat treatments at 350 °C for 2 h which results in an estimated volume loading of 12 %. The infiltration methodology is described elsewhere [7]. High temperature X-ray diffraction (HTXRD) was employed to confirm the perovskite phase and detect any possible secondary phases (STOE Theta-Theta diffractometer, 40 kV, 30 mA, Cu Kα-radiation). A Zeiss Supra 35 electron microscope was used to study the electrode microstructure.

The CGO10 ink was screen printed (40×40 mm^2) onto 53×53 mm^2 large anode supported cell (ASC) consisting of a Ni:8YSZ support, Ni:8YSZ anode, and a 8YSZ electrolyte and sintered at 1,150 °C. The 50 μm thick, porous CGO10 backbone was infiltrated in exactly the same way as were the symmetrical cells and is thus identical to the electrode of cell B. A LSM current collection layer was finally screen printed on top of the electrode to improve electrical contact. This layer was not sintered prior to testing.

Four identical samples of cell A and cell B were painted with Pt paste (Ferro GmbH) on both sides to ensure electrical contact. The painted cells were connected to current and voltage leads using Pt mesh and were measured with electrochemical impedance spectroscopy (EIS) using either a Solartron-1260 frequency response analyzer or a Hioki impedance analyzer. The measurements were carried out at open circuit voltage (*OCV*), under an ambient air flow of 6 $l h^{-1}$ according to the temperature profile in Fig. 1 and under various oxygen partial pressures (P_{O2}) ranging from 0.06 to 0.6 atm. Data were treated with a linear least square fit program, ZsimpWin3.21 in order to retrieve the polarization (R_P) and serial (R_S) resistances and the capacitance associated with the electrode polarization (C_P). An algorithm to extract the distribution of relaxation times (DRT) of the measured impedance was used in the data analysis [14]. All EIS are corrected for inductive contributions from the test setup, and all resistances are reported with a 95 % confidence interval based on the four measured samples.

The ASC was tested using the Risø SOFC test setup described elsewhere [15]. Glass frames with a glass transition temperature and a softening point of approximately 670 °C and 790 °C, respectively, were used to assemble the anode and cathode gas flow compartments. Gold and nickel mesh were used as contacting and current collect components on the cathode and anode side, respectively. Weight (8 kg) was applied on top of the cell house to ensure gas tight sealants and electrical contact. The flow compartments were sealed at 850 °C for 2 h prior to anode reduction in 9 % H_2 in N_2 for 2 h and 4 % H_2O in H_2 for 1 h. All EIS measurements are corrected for inductive contributions from the test setup. The cell was tested from 850–650 °C with

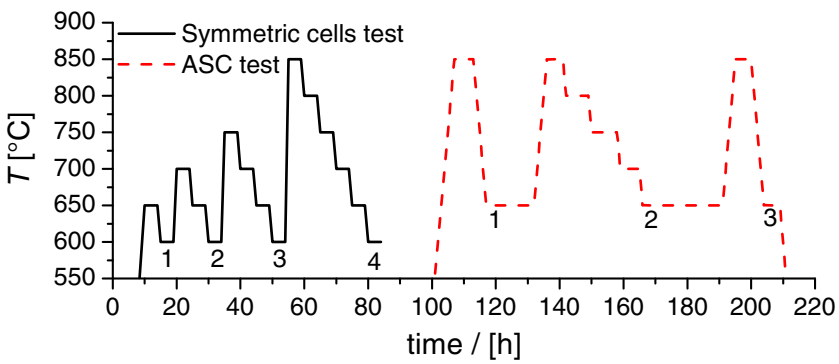

Fig. 1 Experimental temperature profiles of both the symmetrical and *ASC* test. The ramp rate was set to 1 °C min^{-1}

50 °C increments using *i–v* polarization and EIS measurements under a total air flow of 140 lh^{-1} to the cathode side and 24 lh^{-1} H_2 with 20 % humidity to anode side. The cell was tested according to temperature profile in Fig. 1.

Results

Figure 2 plots the X-ray diffractogram measured on cell B at 600 to 850 °C. No significant difference with respect to crystal phase between cell A and cell B was found The results confirmed that the degree of the infiltrate in cell B consisting of the perovskite phase increased at higher sintering temperature. The results show further that there is still a substantial degree of secondary phases even after heat treatment at 850 °C. This appears to consist of cubic SrO. Secondary phases were also reported in a paper by Samson et al. which discusses this aspect in more detail [6]. The presence of secondary phases makes it difficult to conclude the exact composition of the perovskite phase. However, it is plausible to assume that the strontium content is lower than the nominal composition $(La_{0.6}Sr_{0.4})_{0.99}CoO_3$ if the secondary phase consists of SrO.

Figure 3 shows SEM micrographs of Cell A after being heated to 650 °C (a) and 850 °C (b) and demonstrates that the entire thickness of backbone is covered with nanoparticles all the way into the electrolyte. Additionally, the figure confirms that the crystallite size of the infiltrated electro-catalyst in cell A increases at higher sintering temperature. No significant difference in crystallite size was found between cell A and cell B.

Figure 4 shows the Nyquist plots measured on cell A at 600 °C and ambient air after treatment at different maximum temperatures (see Fig. 1). The first EIS measurement at 600 °C revealed R_P values as low as 61±3 mΩ cm^2 and 106±18 mΩ cm^2 for cell A and cell B, respectively. The

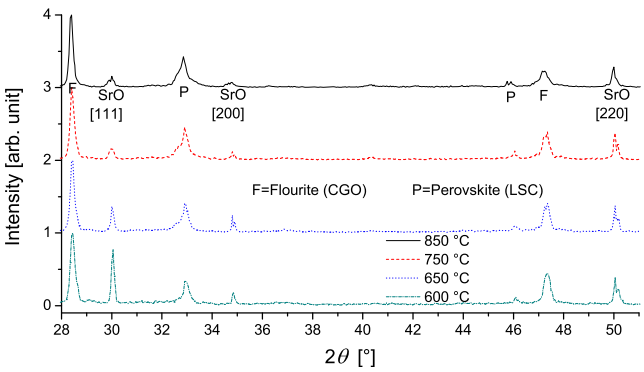

Fig. 2 High temperature XRD patterns of cell B. The peaks P and F corresponds to the perovskite (LSC) and fluorite (CGO) structures, respectively. A secondary phase, believed to consist of cubic SrO, appears to decrease with increasing *T*, while the perovskite peak is seen to increase with increasing *T*

activation energy (E_A) for R_P of cell A for R_P of cell B was calculated to 1.0 and 1.1 eV, respectively. There was no significant change in E_A with the maximum temperature.

Figure 5 plots R_S and R_P of cell A and cell B measured at 600 °C and *OCV* after treatment at different maximum temperatures. The results demonstrate that the electrochemical response of cell A is relatively stable with a small increase in R_P and a small gradual decrease in R_S with increasing maximum *T*. For cell B, a strong increase in both R_P and R_S is seen after heated to 850 °C. It plots further the capacitance, C_P, of the electrode response of both cell A and cell B. The results show a gradual increase in C_P for both cells.

Figure 6 plots the the P_{O2} dependence of two samples of cell A. The main electrode response was found to be approximately $R_P \propto (P_{O2})^{-n}$ with n=0.21±0.02. These results are in close agreement to what was reported in the aforementioned study [6]. Previous papers have found a P_{O2} dependence of the resistance associated with oxygen diffusion of n=0.38±0.03 for single phase porous LSC electrodes [16] and n=0.5 for thin dense LSC electrodes [17]. A second RQ response showed up at low P_{O2} and *f*. The resistance of this low frequency response (R_{GAS}) had a strong P_{O2} dependence. It was found to be independent on *T* and to have a very high capacitance of above 1 F cm^{-2}. This strongly indicates that this resistance is related to a concentration polarization, possibly related to the experimental setup. This response will not be discussed further as it is not directly related to the electrode kinetics.

The increase in resistance with thermal cycling was also seen in the single cell test of the ASC. The results, reported in Fig. 7, show an increase in the ASR at 650 °C with about 35 % and 15 % after the two consecutive thermal cycles to 850 °C (see Fig. 8). AC impedance recorded at *OCV* (Fig. 8) showed that both R_P and R_S increased as a consequence of thermal cycling, in accordance with the results from the tests of cell B.

Figure 9 plots the distribution of relaxation times DRT of cell A, cell B, and the ASC at 650 °C after thermal cycling according to Fig. 1. From the data of cell A and cell B, it is observed that the summit frequency of the main electrode process shifts from about ~20–30 to 3–4 kHz as a result of the thermal treatment. From the data of the ASC, a minor peak can be observed at around 3–4 kHz after the first cycle to 850 °C, in accordance with cell A and cell B.

Discussion

Electrode kinetics

The weaker P_{O2} dependence of infiltrated electrodes as compared to micrometer sized LSC electrodes indicates that

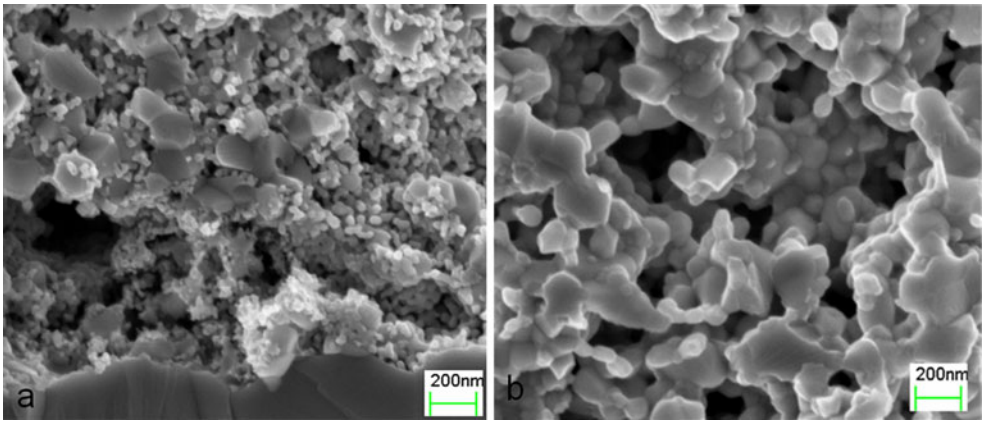

Fig. 3 **a** SEM micrographs of cell A heated to 650 °C for 2 h. **b** Cell A after test and thus heated to maximum 850 °C. Note the increase in particle size with increasing maximum temperature

the oxygen exchange kinetics is mechanistically different for infiltrated electrodes compared to conventional screen printed ones. Additionally, the reaction mechanism of mixed conducting oxygen electrodes are often described as co-limited by the surface exchange reaction (k_{EX}) and oxygen vacancy diffusion (D_V) which is expected to give rise to either a Gerischer- or a finite length Warburg impedance characteristics [18, 19]. However, such features were not observed in the impedance spectra of neither cell A nor cell B. Finally, the capacitance of the electrode response is substantially lower than the typical *chemical capacitance* of single phase LSC cathodes. This can range up to 0.1–1 Fcm^{-2} as a consequence of oxygen non-stoichiometric changes in the bulk [20].

It has been shown using conductivity relaxation data that the kinetic constant for the oxygen surface exchange reaction (k_{EX}) of LSC has a relatively strong P_{O2} dependence ($k_{EX} \propto (P_{O2})^{-n}$ with n approximately equal to 0.5 [21, 22]. In contrast, the oxygen vacancy diffusion is relatively independent on P_{O2}. de Souza et. al. [23, 24] have determined k_{EX} and D_V with the isotope exchange/depth profiling technique and found a strong correlation between the two constants irrespective of material. It was later argued that this correlation could only be rationalized if oxygen incorporation into the bulk is the rate determining elementary step (rds) of the oxygen exchange reaction [25]. One of the arguments was that this is the only elementary step involving oxygen vacancies.

This argument is not necessarily valid. Adler et al. [26] have developed a rigorous kinetic model based on transitions state theory and non-equilibrium thermodynamics. By fitting the model to available non-stoichiometry data, the authors argued that in the specific case of LSC, oxygen dissociation at two adjacent oxygen vacancies is the rds. This has later been supported by density functional theory (DFT) calculations [27]. A P_{O2} dependence, $R_P \propto (P_{O2})^{-n}$ with n=0.5, has repeatedly been observed for LSM electrodes. This dependence was further interpreted as an effect of a dissociation limited reaction [3, 28, 29]. A P_{O2} dependence of 0.5 has also been found for the impedance of conventional LSC electrodes if one takes into account the P_{O2} dependence of oxygen vacancy concentration ($1/R = [V_O^{\cdot\cdot}] \times P_{O2}^{1/2}$) [21]. The weaker P_{O2} dependence of cell A could therefore be interpreted as if dissociation is not rate limiting the overall reaction of LSC infiltrated cathodes to the same degree as conventional micrometer-sized ones.

The size of the nano-crystals, and thus the bulk volume of LSC, is substantially smaller for infiltrated cathodes as opposed to conventional porous ones synthesized from pre-sintered micrometer sized powder. This means that the *chemical capacitance* of infiltrated LSC cathodes should be lower than normal single phase LSC electrodes. More importantly, the characteristic length ($L_C = (D_V)/k_{EX}$) of LSC has been determined to several micrometers thus substantially larger than the size of these LSC nano-particles [30]. The oxygen nonstoichiometry of LSC nano-particles

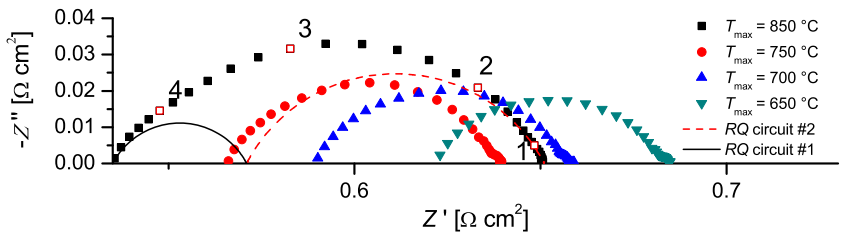

Fig. 4 Nyquist plots showing the impedance measured on cell A at 600 °C and ambient air after treatment at different maximum temperatures (see Fig. 1). Numbers denote $^{10}\log f$. The lines represent the depressed semi-circles of two *RQ* circuit elements in parallel. These represent a typical CNLS equivalent circuit fit to the impedance measured after 850 °C

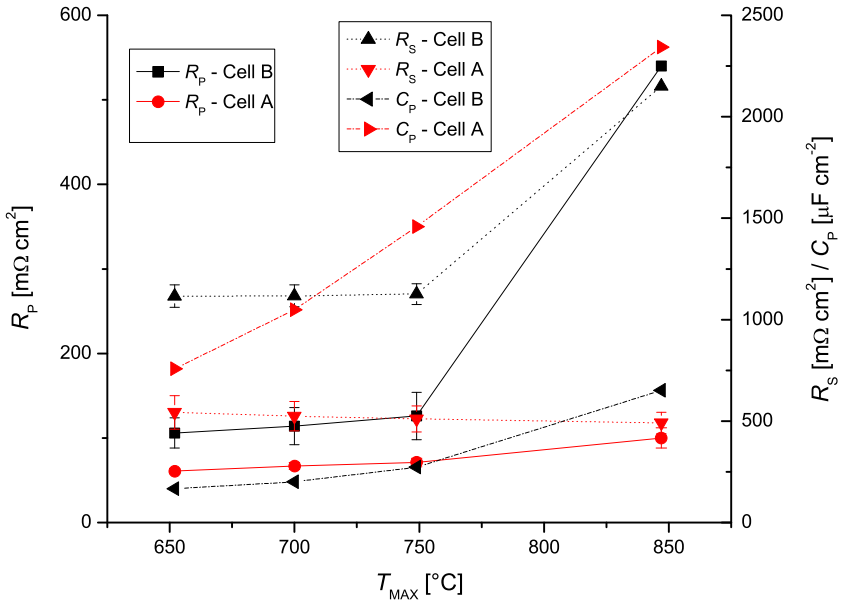

Fig. 5 R_S, R_P and C_P as function of maximum sintering temperature measured at 600 °C in ambient air. The figure illustrates that R_S and R_P of cell A is substantially more stable towards increasing temperatures as compared to cell B

can therefore be assumed to be in equilibrium which in turn suggests that the *chemical capacitance* does not arise as a consequence. Another effect is that oxide ion diffusion is most likely fast enough not to contribute to the electrode resistance. A negligible resistive contribution from oxide ion diffusion through MIEC thin films has previously been shown for LSCF electrodes [31].

The capacitance of an oxygen electrode controlled by adsorption/surface diffusion has been reported to ~10^{-3} F cm^{-2} [32], whereas the double layer capacitance for a true interfacial O^{2-} charge transfer processes in the vicinity of the SOFC electrode/electrolyte/air three phase boundaries (TPB) is typically about 10^{-5}–10^{-6} F cm^{-2} [33]. The capacitance (C_P) of both cell A and cell B were found to be somewhere in between that typically seen for

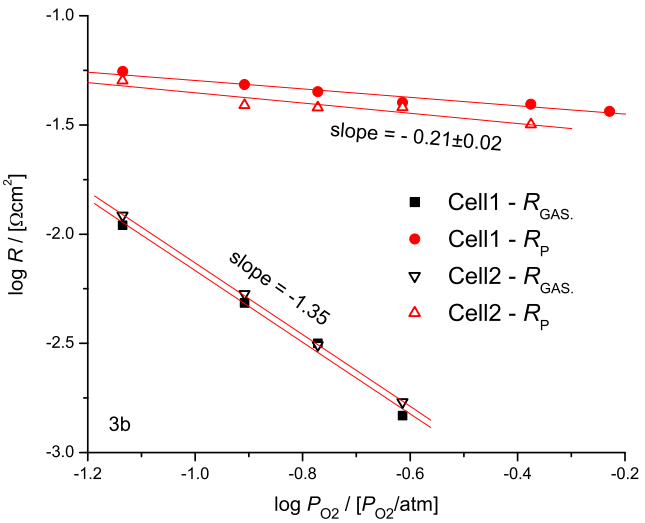

Fig. 6 P_{O2} dependence of R_P and R_{GAS} of two identical samples of cell A measured at 750 °C after treatment at 850 °C

adsorption and charge transfer processes, respectively, making it difficult to draw mechanistic conclusions on the basis of the measured capacitance. However, the idea of a reaction mechanism being limited by a single elementary step, i.e., the bottle neck principle, has for a long time been rightfully questioned when it comes to SOFC electrodes. One of the arguments is that several peaks are often seen when differentiating measured impedance spectra of single electrodes [34].

As an example, in a previous paper studying LCN: CGO10 ($LaCo_{0.4}Ni_{0.6}O_3$) composite electrodes, two processes, clearly separated in the impedance spectra, were found. The spectrum was described using a constant non linear least square (CNLS) equivalent circuit models consisting of a RQ element in series with a Gerischer impedance element. In this case, it was postulated that the reaction proceeded by a mechanism in which oxygen adsorption to and diffusion along the surface is followed by a subsequent charge transfer processes reaction at the TPB. One of the arguments for the hypothetical mechanism was that only the Gerischer impedance decreased when the surface was "modified" by infiltrated LSC nano-particles indicating that only this impedance response was closely related the oxygen adsorption/surface diffusion processes [35].

The relatively low capacitance and comparatively weak P_{O2}-dependence of cell A and cell B could indicate that the reaction proceeds in a similar way for these nano-structured electrodes. The impedance of an electrode reaction controlled by a single process, such as a charge transfer step, is often fitted using a RQ CNLS equivalent circuit, visible as a depressed semi circle in the Nyquist plot. It was not possible to find an equivalent circuit model that could describe the measured impedance consistently throughout the experiments. However, the measured impedance spectra in

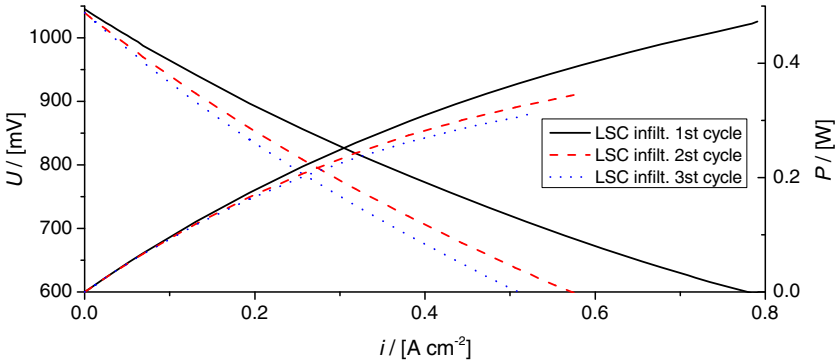

Fig. 7 *i–v* curves and power curves at 650 °C for the ASC tested. x_{H2O}^{A}=0.20, x_{O2}^{C}= 0.21. The cell resistance increases with repeated thermal cycles to 850 °C

Fig. 4 do not seem to be represented by such a simple explanation. This is supported by DRT analysis, plotted in Fig. 9, which shows indications of two peaks after heat treated at 850 °C. Additionally, impedance spectra of similar electrodes have previously been argued to consist of two arcs [6]. The difficulty in discriminating the processes in the time domain can be due to partial overlap in frequency. However, the results suggest the oxygen exchange reaction of this electrode type consist of more than one process contributing the DC resistance.

In fact, the impedance is not very different from that of the conventional micron-sized LCN:CGO10 composite electrode. The difference in this case is that the backbone is an ion conductor (CGO10) with a surface covered by a mixed conductor (LSC). Such a combination of materials opens up the bulk path way and thus a larger fraction of the nano-particle-CGO10 interface than only the TPB. The effect is that diffusion of oxygen can follow either of two ways as illustrated in Fig. 10. Irrespective of which pathway is the predominant, diffusion lengths are substantially shorter compared to electrodes made of micron-sized particles for which we often see Gerischer/Warburg type impedance arising as a consequence of diffusion limitations.

Electrode stability

The increase in R_P with maximum sintering temperature, despite the expected positive effect from an increasing degree of the LSC perovskite phase (see Fig. 2), is well known [6, 8]. Operating these in situ sintered nano-structured electrodes may thus raise concerns about the electrode stability compared to conventional pre-sintered cathodes, which are structurally and chemically "stabilized" at a few hundred degrees above the SOFC operating temperatures.

Perhaps the most plausible reason for the increase in R_P with maximum temperature is nano-particle coarsening which decreases their surface area available for oxygen reduction. Growth of the infiltrated LSC particles with higher maximum temperature is also evident from Fig. 3 which further supports a correlation between R_P of the infiltrated electrodes and the size of its constituting nano-particles. Similar correlations have also been obtained for electrodes with LSM infiltrated into an 8YSZ backbone [36]. However, there could also be other reasons for the correlation between maximum temperature and electrochemical performance. Several reports have correlated lower performance with segregation of strontium to the cathode surface [37, 38]. Additionally, Mogensen et al. [12] have argued that infiltrated nano-particles can react with glassy impurities which otherwise may block the surface or change the surface chemistry of the TPB region. The latter suggestion was supported by the observation of change in the Sr chemistry by impregnation of ceria nano-particles [39]. As redistribution of strontium cations and impurity migration towards, and passivation of, the surface are thermally activated processes, high temperature treatment may then reduce the catalytic activity of the nano-particle surface.

LSC is a very good electronic conductor, especially in contrast to the oxides La_2O_3, SrO, and CoO [40], but the electrode is nevertheless expected to suffer to some degree from current constriction due to the small loading of electronic conducting materials. The higher degree of the LSC phase which is formed after treatment at higher T (see Fig. 2) is thus expected to improve R_S of these electrodes.

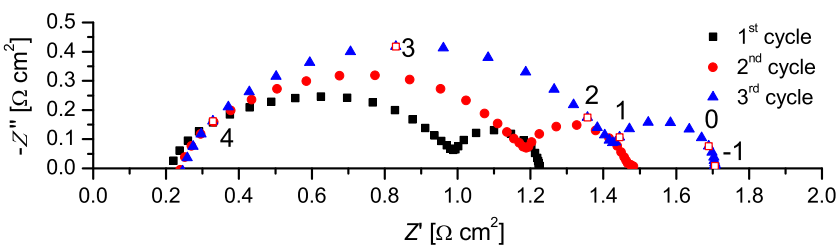

Fig. 8 Nyquist plots of the impedance recorded at *OCV* and 650 °C of the ASC after repeated thermal cycles to 850 °C. x_{H2O}^{A}=0.20, x_{O2}^{C}=0.21. Numbers denote $^{10}\log f$

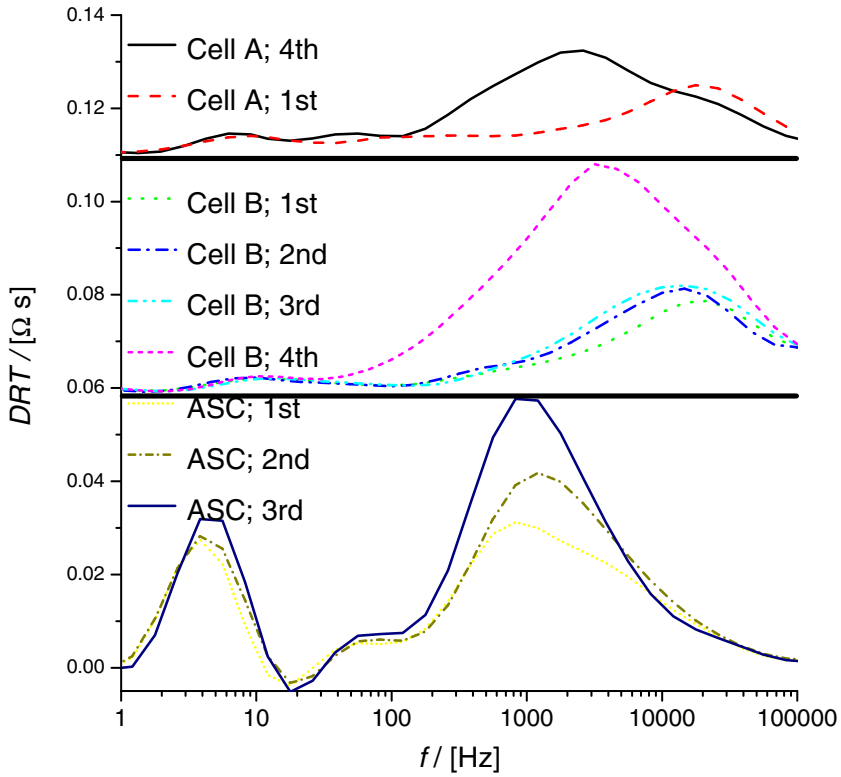

Fig. 9 *DRT* of cell A, cell B and the ASC at 650 °C after thermal cycling according to Fig. 1

Additionally, enhanced percolation and particle necking will improve the microstructure in terms of electronic conductivity. Evidence of such a trend was also found for cell A which showed a decrease in R_S with increasing maximum heat treatment temperature (see Fig. 5). In contrast, cell B demonstrates an opposite behavior with a strong increase in R_S when heated to 850 °C. This suggests that a thermally activated process occurs that has a negative impact on the serial resistance of cell B counteracting the positive effect of LSC formation. The correlated increase in R_P and R_S of cell B during the heating cycle implies that this degradation process will have detrimental effects on both the electrode and electrolyte performance. Since cell B is supported by an 8YSZ electrolyte, one explanation could be that the innermost LSC nano-particles react with 8YSZ to form insulating phases of $SrZrO_3$ and $La_2Zr_2O_7$. Additionally, the Sr activity and mobility is relatively high in LSC allowing it to diffuse along grain boundaries to the YSZ interface [41]. Such a reaction is known to occur between LSC and YSZ at >900 °C as evidenced by XRD for conventional powder [42] and for infiltrated electrodes [43]. In fact, Peters has used thermodynamically modeling to argue that it occurs at temperature >500 °C and argued that lack of evidence from, e.g., XRD is due to slow kinetics at low *T* [44].

An increase in resistance as a result of thermal cycling was also found in the ASC test as seen in Figs. 7 and 8. It is important to note that the first measurement is carried out after treatment for about 7 h at 850 °C at which the cell is sealed and contacted. It is possible to observe a small peak at 3–4 kHz in the DRT of the ASC (see Fig. 9) which corresponds well to the summit frequency of cell A and cell B after sintering at 850 °C. The summit frequency shifts towards lower frequencies as the cathode resistance continues to increase and start to overlap with the anode response, earlier argued to occur at ~1 kHz for this cell type [45]. This makes it very difficult to conclude to which degree the

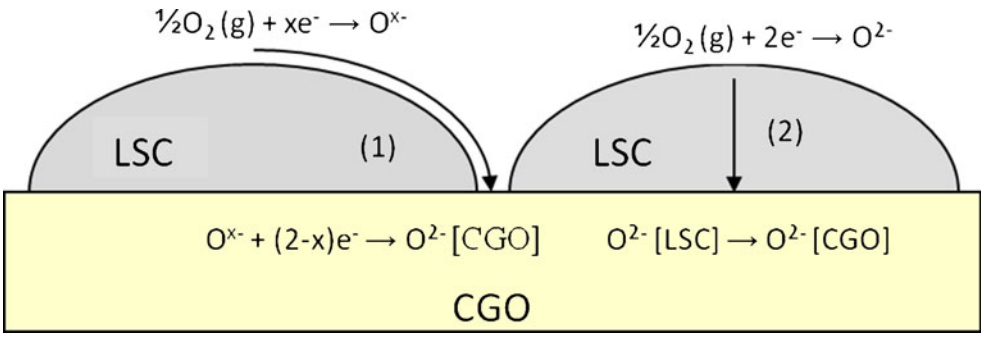

Fig. 10 Illustration of hypothetical reaction pathways for this specific electrode structure

increase in resistance is an effect of the observed cathode degradation.

Whether the decrease in performance is due to thermal cycling or simply an effect of being kept at high temperature for a long time is difficult to conclude. The results show nevertheless that the innermost LSC nano-particles appear comprise an active region of the cathode and that a CGO10 barrier is required if this in situ sintered nano-structured LSC electrode is to be used in SOFCs.

Conclusion

Electrodes consisting of a porous CGO10 scaffold impregnated with nano-sized LSC particles were found to possess high electro-catalytic activity towards oxygen reduction resulting in a R_P as low as 35 mΩ cm^2 at 650 °C. Increasing the electrode sintering temperature increased both the size of the nano-particles and the degree to which they consist of the LSC perovskite phase. EIS measurements found an increase in R_P as an effect of this chemical and structural change. Furthermore, the increase in R_P was significantly stronger for the cell in which the electrolyte was made of YSZ instead of CGO10. The results suggested that the innermost LSC nano-particles had reacted with the YSZ electrolyte.

The electrode was successfully integrated into an anode supported cell with an ASR of 540 mΩ cm^2 at 650 °C. This value increased when the cell was thermal cycled to 850 °C further indicating the thermal instability of the cathode when applied directly onto YSZ. The results demonstrate the requirement of a CGO10 barrier to prevent any reaction between the LSC nano-particles and the 8YSZ electrolyte if the cell is to be operated at higher temperatures.

References

1. Adler SB (2004) Chem Rev 104:4791–4843
2. Hjalmarsson P, Søgaard M, Mogensen M (2008) Solid State Ionics 179:1422–1426
3. Takeda Y, Kanno R, Noda M, Tomida Y, Yamamoto O (1987) J Electrochem Soc 134:2656–2661
4. Yamamoto O, Takeda Y, Kanno R, Noda M (1987) Solid State Ionics 22:241–246
5. Chen XY, Yu JS, Adler SB (2005) Chem Mater 17:4537–4546
6. Samson A, Søgaard M, Knibbe R, Bonanos N (2011) J Electrochem Soc 158:B650–B659
7. Sholklapper TZ, Lu C, Jacobson CP, Visco SJ, De Jonghe LC (2006) Electrochem Solid-State Lett 9:A376–A378
8. Sholklapper TZ, Radmilovic V, Jacobson CP, Visco SJ, De Jonghe LC (2007) Electrochem Solid-State Lett 10:B74–B76
9. Shah M, Nicholas JD, Barnett SA (2009) Electrochem Commun 11:2–5
10. Shah M, Barnett SA (2008) Solid State Ionics 179:2059–2064
11. Nicholas JD, Barnett SA (2010) J Electrochem Soc 157:B536–B541
12. Mogensen M, Søgaard M, Blennow P, Hansen KK (2008) The Action of Nano-Particles in SOFC Electrodes. In: Steinberger-Wilckens R, Bossel U (ed) Proc 8th Eur Solid Oxide Fuel Cell Forum
13. Vohs JM, Gorte RJ (2009) Adv Mater 21:943–956
14. Schichlein H, Muller AC, Voigts M, Krugel A, Ivers-Tiffee E (2002) J Appl Electrochem 32:875–882
15. Hendriksen PV, Mogensen M (2003) Chapter 10: Testing of electrodes, cells and short stacks, high temperature solid oxide fuel cells: Fundamentals, design and applications. In: Kendall K, Singhal S (ed) Elsevier Advanced Technology, Oxford, p 261
16. Hjalmarsson P, Søgaard M, Mogensen M (2009) Solid State Ionics 180:1395–1405
17. Imanishi N, Matsumura T, Sumiya Y, Yoshimura K, Hirano A, Takeda Y, Mori D, Kanno R (2004) Solid State Ionics 174:245–252
18. Adler SB (1998) Solid State Ionics 111:125–134
19. Nielsen J, Jacobsen T, Wandel M (2011) Electrochim Acta 56:7963–7974
20. Adler SB, Lane JA, Steele BCH (1996) J Electrochem Soc 143:3554–3564
21. Søgaard M, Hendriksen PV, Mogensen M, Poulsen FW, Skou E (2006) Solid State Ionics 177:3285–3296
22. van der Haar LM, den Otter MW, Morskate M, Bouwmeester HJM, Verweij H (2002) J Electrochem Soc 149:J41–J46
23. De Souza RA, Kilner JA (1999) Solid State Ionics 126:153–161
24. De Souza RA, Kilner JA (1998) Solid State Ionics 106:175–187
25. Merkle R, Maier J, Bouwmeester HJM (2004) Angew Chem Int Ed 43:5069–5073
26. Adler SB, Chen XY, Wilson JR (2007) J Catal 245:91–109
27. Merkle R, Mastrikov YA, Heifets E, Kotomin EA, Kukla M, Maier J (2009) Oxygen incorporation reaction into mixed conducting perovskites: a mechanistic analysis for (La,Sr)MnO3 based on DFT calculations. In: Anonymous (ed) ECS Transactions, pp 2753–2760
28. Siebert E, Hammouche A, Kleitz M (1995) Electrochim Acta 40:1741–1753
29. Van Herle J, McEvoy AJ, Ravindranathan TK (1996) Electrochim Acta 41:1447–1454
30. Bouwmeester HJM, Kruidhof H, Burggraaf AJ (1994) Solid State Ionics 72:185–194
31. Fleig J, Baumann FS, Brichzin V, Kim HR, Jamnik J, Cristiani G, Habermeier HU, Maier J (2006) Fuel Cells 6:284–292
32. Kawada T, Suzuki J, Sase M, Kaimai A, Yashiro K, Nigara Y, Mizusaki J, Kawamura K, Yugami H (2002) J Electrochem Soc 149:E252–E259
33. Robertson NL, Michaels JN (1991) J Electrochem Soc 138:1494–1499
34. Ostergard MJL, Mogensen M (1993) Electrochim Acta 38:2015–2020
35. Hjalmarsson P, Mogensen M (2011) J Power Sources 196:7237–7244
36. Huang YY, Vohs JM, Gorte RJ (2005) J Electrochem Soc 152: A1347–A1353
37. Baumann FS, Fleig J, Konuma M, Starke U, Habermeier HU, Maier J (2005) J Electrochem Soc 152:A2074–A2079
38. Simner SP, Anderson MD, Engelhard MH, Stevenson JW (2006) Electrochem Solid State Lett 9:A478–A481
39. Knöfel C, Wang H, Thyden KTS, Mogensen M (2011) Solid State Ionics 195:36–42
40. Mineshige A, Inaba M, Yao TS, Ogumi Z, Kikuchi K, Kawase M (1996) J Solid State Chem 121:423–429
41. Yokokawa H, Sakai N, Horita T, Yamaji K, Brito ME, Kishimoto H (2008) J Alloys Comp 452:41–47
42. Labrincha JA, Frade JR, Marques FMB (1993) J Mater Sci 28:3809–3815
43. Küngas R, Bidrawn F, Vohs JM, Gorte RJ (2010) Electrochem Solid-State Lett 13:B87–B90
44. Peters C (2008) Grain-size effects in nanoscaled electrolyte and cathode thin films for SOFC. Karlsruhe Scientific Publishing, Karlsruhe
45. Barfod R, Mogensen M, Klemensø T, Hagen A, Liu Y, Hendriksen PV (2007) J Electrochem Soc 154:B371–B378